

See discussions, stats, and author profiles for this publication at: <https://www.researchgate.net/publication/6822794>

Retianl Vessel Segmentation Using the 2-D Gabor Wavelet and Supervised Classification

Article in IEEE Transactions on Medical Imaging · October 2006

DOI: 10.1109/TMI.2006.879967 · Source: PubMed

CITATIONS

1,172

READS

2,406

5 authors, including:



[Jorge de Jesus Gomes Leandro](#)

University of São Paulo

28 PUBLICATIONS 1,701 CITATIONS

[SEE PROFILE](#)



[Roberto Marcondes Cesar Junior](#)

University of São Paulo

163 PUBLICATIONS 3,559 CITATIONS

[SEE PROFILE](#)



[Herbert F Jelinek](#)

Charles Sturt University

396 PUBLICATIONS 6,972 CITATIONS

[SEE PROFILE](#)



[Michael J. Cree](#)

The University of Waikato

136 PUBLICATIONS 4,091 CITATIONS

[SEE PROFILE](#)

Some of the authors of this publication are also working on these related projects:



Morphological Changes of Cardiac Muscle in association with progression of Disease [View project](#)



Diabetes complications screening and use of engineering solutions [View project](#)

Retinal Vessel Segmentation Using the 2-D Morlet Wavelet and Supervised Classification

João V. B. Soares, Jorge J. G. Leandro, Roberto M. Cesar-Jr., Herbert F. Jelinek, and Michael J. Cree, *Senior Member, IEEE*

Abstract—We present a method for automated segmentation of the vasculature in retinal images. The method produces segmentations by classifying each image pixel as *vessel* or *non-vessel*, based on the pixel's feature vector. Feature vectors are composed of the pixel's intensity and continuous two-dimensional Morlet wavelet transform responses taken at multiple scales. The Morlet wavelet is capable of tuning to specific frequencies, thus allowing noise filtering and vessel enhancement in a single step. We use a Bayesian classifier with class-conditional probability density functions (likelihoods) described as Gaussian mixtures, yielding a fast classification, while being able to model complex decision surfaces and compare its performance with the linear minimum squared error classifier. The probability distributions are estimated based on a training set of labeled pixels obtained from manual segmentations. The method's performance is evaluated on publicly available DRIVE [1] and STARE [2] databases of manually labeled non-mydratic images. On the DRIVE database, it achieves an area under the receiver operating characteristic (ROC) curve of 0.9598, being slightly superior than that presented by the method of Staal *et al.* [1].

Index Terms—Fundus, Morlet, pattern classification, retina, vessel segmentation, wavelet.

I. INTRODUCTION

OPTIC fundus (Fig. 1(a)) assessment has been widely used by the medical community for diagnosing vascular and non-vascular pathology. Inspection of the retinal vasculature may reveal hypertension, diabetes, arteriosclerosis, cardiovascular disease and stroke [3]. Diabetic retinopathy is a major cause of adult blindness due to changes in blood vessel structure and distribution such as new vessel growth (proliferative diabetic retinopathy) and requires laborious analysis from a specialist [4]. Endeavoring to reduce the effect of proliferative diabetic retinopathy includes obtaining and analyzing images of the optic fundus at regular intervals such as every six months to a year. Early recognition of changes



(a) Inverted green channel of non-mydratic fundus image. (b) Pre-processed image with extended border. The original image limit is indicated for illustration.

Fig. 1. Fundus image pre-processing for removing undesired border effects.

to the blood vessel patterns can prevent major vision loss as early intervention becomes possible [5], [6].

To provide the opportunity for initial assessment to be carried out by community health workers, computer based analysis has been introduced, which includes assessment of the presence of microaneurysms and changes in the blood flow/vessel distribution due to either vessel narrowing, complete occlusions or new vessel growth [7]–[9].

An automatic assessment for blood vessel anomalies of the optic fundus initially requires the segmentation of the vessels from the background, so that suitable feature extraction and processing may be performed. Several methods have been developed for vessel segmentation, but visual inspection and evaluation by receiver operating characteristic (ROC) analysis shows that there is still room for improvement [10], [11]. In addition, it is important to have segmentation algorithms that do not critically depend on configuring several parameters so that untrained community health workers may utilize this technology. These limitations of the state-of-the-art algorithms have motivated the development of the framework described here, which only depends on manually segmented images.

Many different approaches for automated vessel segmentation have been reported. The papers [12]–[18] present vessel tracking methods to obtain the vasculature structure, along with vessel diameters and branching points. Tracking consists of following vessel center lines guided by local information, usually trying to find the path which best matches a vessel profile model. The use of deformable models also shows

©2006 IEEE. Personal use of this material is permitted. However, permission to reprint/republish this material for advertising or promotional purposes or for creating new collective works for resale or redistribution to servers or lists, or to reuse any copyrighted component of this work in other works must be obtained from the IEEE.

This work was supported by CNPq (131403/2004-4, 300722/98-2 and 474596/2004-4), FAPESP (99/12765-2), the Australian Diabetes Association and the CSU CoS.

J. Soares, J. Leandro, and R. Cesar-Jr. are with the Institute of Mathematics and Statistics - University of São Paulo - USP, Brazil (e-mails: {joao, jleandro, cesar}@vision.ime.usp.br).

H. Jelinek is with the School of Community Health, Charles Sturt University, Australia (e-mail: hjelinek@csu.edu.au).

M. Cree is with the Department of Physics and Electronic Engineering, University of Waikato, Hamilton, New Zealand (e-mail: cree@waikato.ac.nz).

promising results in [19]–[22]. In [2], [23], [24], matched filters are used to emphasize blood vessels. An improvement is obtained in [2] by a region-based threshold probing of the matched filter response. Multithreshold probing is directly applied to the images in [25]. A non-linear filter that enhances vessels by exploiting properties of the vessel profiles is introduced in [26]. Along this line is the use of mathematical morphology filtering in [27], [28], coupled with curvature evaluation. In [29], multi-scale curvature and border detection are used to drive a region growing algorithm.

Supervised methods for pixel classification have been shown in [1], [30], [31]. In [30], feature vectors are formed by gray-scale values from a window centered on the pixel being classified. A window of values is also used in [31], but the features used are a principal component transformation of RGB values and edge strength. In [1], ridge detection is used to form line elements and partition the image into patches belonging to each line element. Pixel features are then generated based on this representation. Many features are presented and a feature selection scheme is used to select those which provide the best class separability.

Previously, we have shown promising preliminary results using the continuous wavelet transform (CWT) [32], [33] and integration of multi-scale information through supervised classification [34]. Here we improve on those methods using a Bayesian classifier with Gaussian mixture models as class likelihoods and evaluate performances with ROC analysis. ROC analysis has been used for evaluation of segmentation methods in [1], [2], [25] and comparison of some of the cited methods in [10], [11].

In our approach, each pixel is represented by a feature vector including measurements at different scales taken from the continuous two-dimensional Morlet wavelet transform. The resulting feature space is used to classify each pixel as either a *vessel* or *non-vessel* pixel. We use a Bayesian classifier with class-conditional probability density functions (likelihoods) described as Gaussian mixtures, yielding a fast classification, while being able to model complex decision surfaces and compare its performance with the linear minimum squared error classifier.

Originally devised for suitably analyzing non-stationary and inhomogeneous signals, the time-scale analysis took place to accomplish unsolvable problems within the Fourier framework, based on the continuous wavelet transform (CWT). The CWT is a powerful and versatile tool that has been applied to many different image processing problems, from image coding [35] to shape analysis [36]. This success is largely due to the fact that wavelets are especially suitable for detecting singularities (e.g. edges and other visual features) in images [37], extracting instantaneous frequencies [38], and performing fractal and multi-fractal analysis. Furthermore, the wavelet transform using the Morlet wavelet, also often referred to as Gabor wavelet, has played a central role in increasing our understanding of visual processing in different contexts from feature detection to face tracking [39]. The Morlet wavelet is directional and capable of tuning to specific frequencies, allowing it to be adjusted for vessel enhancement and noise filtering in a single step. These nice characteristics motivate

the adoption of the Morlet wavelet in our proposed framework.

This work is organized as follows. The databases used for tests are described in Subsection II-A. Subsection II-B presents our segmentation framework based on supervised pixel classification. In Subsection II-C the feature generation process is described, including the 2-D CWT and Morlet wavelet. Our use of supervised classification and the classifiers tested are presented in Subsection II-D. ROC analysis for performance evaluation is described in Subsection II-E and results are presented in Section III. Discussion and conclusion are in Section IV.

II. MATERIALS AND METHODS

A. Materials

There are different ways of obtaining ocular fundus images, such as with non-mydiatic cameras, which do not require the dilation of the eyes through drops, or through angiograms using fluorescein as a tracer [5]. We have tested our methods on angiogram gray-level images and colored non-mydiatic images [32], [34]. Here, our methods are tested and evaluated on two publicly available databases of non-mydiatic images and corresponding manual segmentations: the DRIVE [1] and STARE [2] databases.

The DRIVE database consists of 40 images (7 of which present pathology), along with manual segmentations of the vessels. The images are captured in digital form from a Canon CR5 non-mydiatic 3CCD camera at 45° field of view (FOV). The images are of size 768×584 pixels, 8 bits per color channel and have a FOV of approximately 540 pixels in diameter. The images are in compressed JPEG-format, which is unfortunate for image processing but is commonly used in screening practice.

The 40 images have been divided into a training and test set, each containing 20 images (the training set has 3 images with pathology). They have been manually segmented by three observers trained by an ophthalmologist. The images in the training set were segmented once, while images in the test set were segmented twice, resulting in sets A and B. The observers of sets A and B produced similar segmentations. In set A, 12.7% of pixels were marked as vessel, against 12.3% vessel for set B. Performance is measured on the test set using the segmentations of set A as ground truth. The segmentations of set B are tested against those of A, serving as a human observer reference for performance comparison.

The STARE database consists of 20 digitized slides captured by a TopCon TRV-50 fundus camera at 35° FOV. The slides were digitized to 700×605 pixels, 8 bits per color channel. The FOV in the images are approximately 650×550 pixels in diameter. Ten of the images contain pathology. Two observers manually segmented all images. The first observer segmented 10.4% of pixels as vessel, against 14.9% vessels for the second observer. The segmentations of the two observers are fairly different in that the second observer segmented much more of the thinner vessels than the first one. Performance is computed with the segmentations of the first observer as ground truth.

B. General framework

The image pixels of a fundus image are viewed as objects represented by feature vectors, so that we may apply statistical classifiers in order to segment the image. In this case, two classes are considered, i.e. *vessel* \times *non-vessel* pixels. The training set for the classifier is derived by manual segmentations of training images, i.e. pixels segmented by hand are labeled as *vessel* while the remaining pixels are labeled as *non-vessel*. This approach allows us to integrate information from wavelet responses at multiple scales in order to distinguish pixels from each class.

C. Pixel features

When the RGB components of the non-mydratic images are visualized separately, the green channel shows the best vessel/background contrast (Fig. 1(a)), whereas, the red and blue channels show low contrast and are very noisy. Therefore, the green channel was selected to be processed by the wavelet, as well as to compose the feature vector itself, i.e. the green channel intensity of each pixel is taken as one of its features. For angiograms, the wavelet is applied directly to the gray-level values, which are also used to compose the feature vectors.

1) *Pre-processing*: In order to reduce false detection of the border of the camera's aperture by the wavelet transform, an iterative algorithm has been developed. Our intent is to remove the strong contrast between the retinal fundus and the region outside the aperture (see Fig. 1).

The pre-processing algorithm consists of determining the pixels outside the aperture that are neighbors to pixels inside the aperture and replacing each of their values with the mean value of their neighbors inside the aperture. This process is repeated and can be seen as artificially increasing the area inside the aperture, as shown in Fig. 1(b).

Before the application of the wavelet transform to non-mydratic images, we invert the green channel of the image, so that the vessels appear brighter than the background.

2) *Wavelet transform features*: The notation and definitions in this section follow [40]. The real plane $\mathbb{R} \times \mathbb{R}$ is denoted as \mathbb{R}^2 , and the vectors are represented as bold letters, e.g. $\mathbf{x}, \mathbf{b} \in \mathbb{R}^2$. Let $f \in L^2$ be an image represented as a square integrable (i.e. finite energy) function defined over \mathbb{R}^2 . The continuous wavelet transform $T_\psi(\mathbf{b}, \theta, a)$ is defined as:

$$T_\psi(\mathbf{b}, \theta, a) = C_\psi^{-1/2} \frac{1}{a} \int \psi^*(a^{-1}r_{-\theta}(\mathbf{x} - \mathbf{b}))f(\mathbf{x})d^2\mathbf{x}$$

where C_ψ , ψ , \mathbf{b} , θ and a denote the normalizing constant, analyzing wavelet, the displacement vector, the rotation angle and the dilation parameter (also known as scale), respectively. ψ^* denotes the complex conjugate of ψ .

Combining the conditions for both the analyzing wavelet and its Fourier transform of being well localized in the time and frequency domain plus the requirement of having zero mean, one realizes that the wavelet transform provides a local filtering at a constant rate $\frac{\Delta\omega}{\omega}$, indicating its great efficiency as the frequency increases, i.e. as the scale decreases. This property is what makes the wavelet effective for detection and

analysis of localized properties and singularities [38], such as the blood vessels in the present case.

Among several available analyzing wavelets, for instance, the 2-D Mexican hat and the optical wavelet, we chose the 2-D Morlet wavelet for the purposes of this work, due to its directional selectiveness capability of detecting oriented features and fine tuning to specific frequencies [38], [40]. This latter property is especially important in filtering out the background noise of the fundus images. The 2-D Morlet wavelet is defined as:

$$\psi_M(\mathbf{x}) = \exp(j\mathbf{k}_0\mathbf{x}) \exp\left(-\frac{1}{2}|A\mathbf{x}|^2\right)$$

where $j = \sqrt{-1}$ and $A = \text{diag}[\epsilon^{-1/2}, 1]$, $\epsilon \geq 1$ is a 2×2 diagonal matrix that defines the anisotropy of the filter, i.e. its elongation in any desired direction [38]. The Morlet wavelet is actually a complex exponential modulated Gaussian, where \mathbf{k}_0 is a vector that defines the frequency of the complex exponential.

We have set the ϵ parameter to 8, making the filter elongated and $\mathbf{k}_0 = [0, 3]$, i.e. a low frequency complex exponential with few significant oscillations, as shown in Fig. 2. These two characteristics have been chosen in order to enable the transform to present stronger responses for pixels associated with the blood vessels.

For each considered scale value, we are interested in the response with maximum modulus over all possible orientations, i.e.:

$$M_\psi(\mathbf{b}, a) = \max_\theta |T_\psi(\mathbf{b}, \theta, a)| \quad (1)$$

Thus, the Morlet wavelet transform is computed for θ spanning from 0 up to 170 degrees at steps of 10 degrees and the maximum is taken (this is possible because $|T_\psi(\mathbf{b}, \theta, a)| = |T_\psi(\mathbf{b}, \theta + 180, a)|$). The maximum modulus of the wavelet transform over all angles for multiple scales are then taken as pixel features. $M_\psi(\mathbf{b}, a)$ is shown in Fig. 3 for $a = 2$ and $a = 4$ pixels.

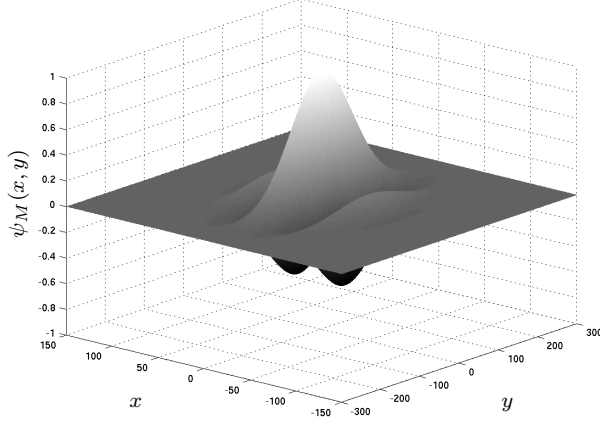
3) *Feature normalization*: Given the dimensional nature of the features forming the feature space, one must bear in mind that this might give rise to errors in the classification process, as the units chosen might affect the distance in the feature space.

A strategy to obtain a new random variable with zero mean and unit standard deviations, yielding, in addition, dimensionless features, is to apply the normal transformation to the feature space. The normal transformation is defined as [36]:

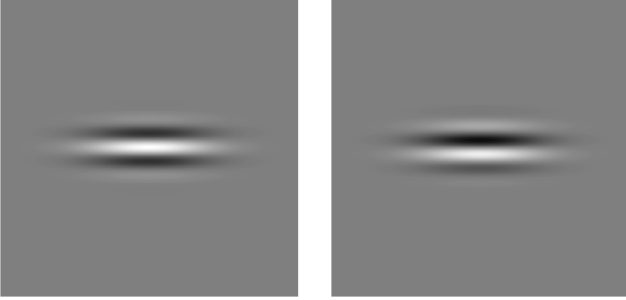
$$\hat{v}_i = \frac{v_i - \mu_i}{\sigma_i}$$

where v_i is the i^{th} feature assumed by each pixel, μ_i is the average value of the i^{th} feature and σ_i is the associated standard deviation.

We have applied the normal transformation separately to each image's feature space, i.e., every image's feature space is normalized by its own means and standard deviations, helping to compensate for intrinsic variation between images (e.g. illumination).



(a) Surface representation of the real part.



(b) Real part.

(c) Imaginary part.

Fig. 2. Different representations for the 2-D Morlet wavelet (ψ_M) with parameters $\epsilon = 8$ and $\mathbf{k}_0 = [0, 3]$.

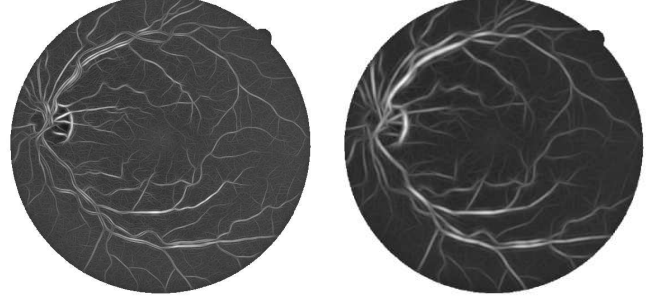
D. Supervised classification for segmentation

Supervised classification has been applied to obtain the final segmentation, with the pixel classes defined as $C_1 = \{\text{vessel pixels}\}$ and $C_2 = \{\text{non-vessel pixels}\}$. In order to obtain the training set, several fundus image have been manually segmented, allowing the creation of a labeled training set into classes C_1 and C_2 (see Subsection II-A). Due to the computational cost of training the classifiers and the large number of samples, we randomly select a subset of the available samples to use for actually training the classifiers. We will present results for two different classifiers, described below.

1) *Gaussian mixture model Bayesian classifier*: We have achieved very good results using a Bayesian classifier in which each class-conditional probability density function (likelihood) is described as a linear combination of Gaussian functions [41], [42]. We will call this the *Gaussian mixture model* (GMM) classifier.

The *Bayes classification rule* for a feature vector \mathbf{v} can be stated in terms of posterior probabilities as

$$\begin{aligned} &\text{Decide } C_1 \text{ if } P(C_1|\mathbf{v}) > P(C_2|\mathbf{v}); \\ &\text{otherwise, decide } C_2 \end{aligned} \quad (2)$$

(a) $M_\psi(\mathbf{b}, 2)$.(b) $M_\psi(\mathbf{b}, 4)$.Fig. 3. Maximum modulus of Morlet wavelet transform over angles, $M_\psi(\mathbf{b}, a)$ (Eq. 1), for scale values of $a = 2$ and $a = 4$ pixels. The remaining parameters are fixed at $\epsilon = 8$ and $\mathbf{k}_0 = [0, 3]$.

We recall *Bayes rule*:

$$P(C_i|\mathbf{v}) = \frac{p(\mathbf{v}|C_i)P(C_i)}{p(\mathbf{v})} \quad (3)$$

where $p(\mathbf{v}|C_i)$ is the class-conditional probability density function, also known as likelihood, $P(C_i)$ is the prior probability of class C_i , and $p(\mathbf{v})$ is the probability density function of \mathbf{v} (sometimes called evidence).

To obtain a decision rule based on estimates from our training set, we apply *Bayes rule* to Eq. 2, obtaining the equivalent decision rule:

$$\begin{aligned} &\text{Decide } C_1 \text{ if } p(\mathbf{v}|C_1)P(C_1) > p(\mathbf{v}|C_2)P(C_2); \\ &\text{otherwise, decide } C_2 \end{aligned}$$

We estimate $P(C_i)$ as N_i/N , the ratio of class i samples in the training set. The class likelihoods are described as linear combinations of Gaussian functions:

$$p(\mathbf{v}|C_i) = \sum_{j=1}^{k_i} p(\mathbf{v}|j, C_i)P_j$$

where k_i is the number of Gaussians modeling likelihood i , P_j is the weight of Gaussian j and each $p(\mathbf{v}|j, C_i)$ is a d -dimensional Gaussian distribution.

For each class i , we estimate the k_i Gaussian parameters and weights with the Expectation-Maximization (EM) algorithm [41]. The EM algorithm is an iterative scheme that guarantees a local maximum of the likelihood of the training data.

GMMs represent a halfway between purely nonparametric and parametric models, providing a relatively fast classification process at the cost of a more expensive training algorithm.

2) *Linear minimum squared error classifier*: We have also tested the linear minimum squared error classifier [41], [42], denoted LMSE. Linear classifiers are defined by a linear decision function g in the d -dimensional feature space:

$$g(\mathbf{v}) = \mathbf{w}^t \mathbf{v} + w_0 \quad (4)$$

where \mathbf{v} is a feature vector, \mathbf{w} is the weight vector and w_0 the threshold.

The classification rule is to decide C_1 if $g(\mathbf{v}) > 0$ and C_2 otherwise. To simplify the formulation, the threshold w_0 is accommodated by defining the extended $(d+1)$ -dimensional vectors $\mathbf{v}' \equiv [\mathbf{v}^T, 1]^T$ and $\mathbf{w}' \equiv [\mathbf{w}^T, w_0]^T$, so that $g(\mathbf{v}) = \mathbf{w}'^T \mathbf{v}'$.

The classifier is determined by finding \mathbf{w}' that minimizes the *sum of error squares* criterion:

$$J(\mathbf{w}') = \sum_{i=1}^N (y_i - \mathbf{v}_i'^T \mathbf{w}')^2$$

where N is the total number of training samples, \mathbf{v}_i' is the extended i^{th} training sample, and y_i its desired output.

The criterion measures the sum of squared errors between the true output of the classifier ($\mathbf{v}_i'^T \mathbf{w}'$) and the desired output (y_i). We have arbitrarily set $y_i = 1$ for $\mathbf{v}_i \in C_1$ and $y_i = -1$ for $\mathbf{v}_i \in C_2$.

Let us define

$$V = \begin{bmatrix} \mathbf{v}_1'^T \\ \mathbf{v}_2'^T \\ \vdots \\ \mathbf{v}_N'^T \end{bmatrix}, \quad \mathbf{y} = \begin{bmatrix} y_1 \\ y_2 \\ \vdots \\ y_N \end{bmatrix}$$

Minimizing the criterion with respect to \mathbf{w}' results in:

$$(V^T V) \hat{\mathbf{w}}' = V^T \mathbf{y} \Rightarrow \hat{\mathbf{w}}' = (V^T V)^{-1} V^T \mathbf{y}$$

In comparison to the GMM classifier, the LMSE classifier has a much faster training process, but is restricted in the sense that it is linear, while GMMs allow for complex decision boundaries. However, as we will show, the results obtained using LMSE are comparable to those using GMMs, representing a reasonable trade-off.

E. Experimental evaluation

The performances are measured using receiver operating characteristic (ROC) curves. ROC curves are plots of true positive fractions versus false positive fractions for varying thresholds on the posterior probabilities. A pair formed by a true positive fraction and a false positive fraction is plotted on the graph for each threshold value (as explained below), producing a curve as in Figs. 6 and 7. The true positive fraction is determined by dividing the number of true positives by the total number of vessel pixels in the ground truth segmentations, while the false positive fraction is the number of false positives divided by the total number of non-vessel pixels in the ground truth. In our experiments, these fractions are calculated over all test images, considering only pixels inside the FOV.

For the GMM classifier, the ROC curve is produced by varying the threshold on the posterior pixel probabilities (see Eq. 3), while the LMSE ROC curve is produced varying the threshold w_0 on the projection of the feature vectors on the discriminant vector (see Eq. 4).

We have tested our methods on the DRIVE and STARE databases with the following settings. The pixel features used for classification were the inverted green channel and its maximum Morlet transform response over angles $M_\psi(\mathbf{b}, a)$ (Eq. 1) for scales $a = 2, 3, 4, 6$ pixels (see Subsection II-C).

For the DRIVE database, the training set was formed by pixel samples from the 20 labeled training images. For the STARE database, leave-one-out tests were performed, i.e., every image is segmented using samples from the other 19 images for the training set. Due to the large number of pixels, in all experiments, one million pixel samples were randomly chosen to train the classifiers. Tests were performed with the LMSE and GMM classifiers. For the GMM classifier, we vary the number $k = k_1 = k_2$ of *vessel* and *non-vessel* Gaussians modeling each class likelihood.

III. RESULTS

Illustrative segmentation results for a pair of images from each database (produced by the GMM classifier with $k = 20$), along with the manual segmentations, are shown in Figs. 4 and 5.

For the DRIVE database, the manual segmentations from set A are used as ground truth and the human observer performance is measured using the manual segmentations from set B, which provide only one true/false positive fraction pair, appearing as a point in the ROC graph (Fig. 6). For the STARE database, the first observer's manual segmentations are used as ground truth, and the second observer's true/false positive fraction pair is plotted on the ROC graph (Fig. 7). The closer an ROC curve approaches the top left corner, the better the performance of the method. A system that agreed completely with the ground truth segmentations would yield an area under the ROC curve $A_z = 1$. However, note that the second sets of manual segmentations do not produce perfect true/false positive fractions, for the manual segmentations evaluated disagree on some of the pixels with the manual segmentations used as ground truth. Thus, the variance between observers can be estimated, helping to set a goal for the method's performance.

The areas under the ROC curves (A_z) are used as a single measure of the performance of each method and are shown in Table I for GMM classifiers of varying k and for the LMSE classifier. For comparison with the manual segmentations, we also measure the accuracies (fraction of correctly classified pixels) of the automatic and manual segmentations. Note that the accuracy and A_z values for the GMM classifier increase with k . The ROC curves for the DRIVE and STARE databases produced using the GMM classifier with $k = 20$, as well as performances for human observers, are shown in Figs. 6 and 7.

We note that the EM training process for the GMMs is computationally more expensive as k increases, while the classification phase is fast. On the other hand, LMSE is very fast for both training and classification, but produces poorer results, as seen in Table I.

IV. DISCUSSION AND CONCLUSION

The Morlet transform shows itself efficient in enhancing vessel contrast, while filtering out noise. Information from

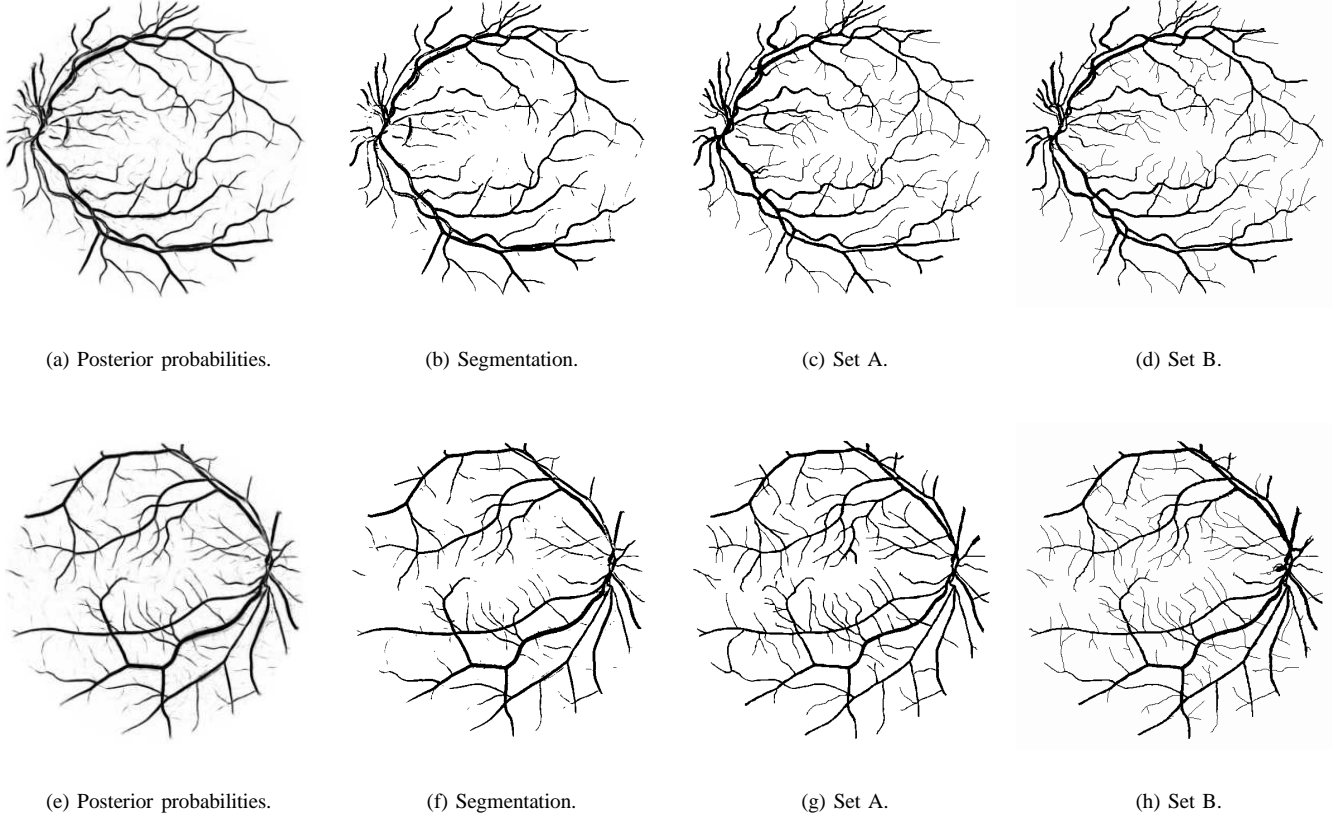


Fig. 4. Results produced by the GMM classifier with $k = 20$ and manual segmentations for two images from the DRIVE database. The top row results are for the image shown in Fig. 1(a).

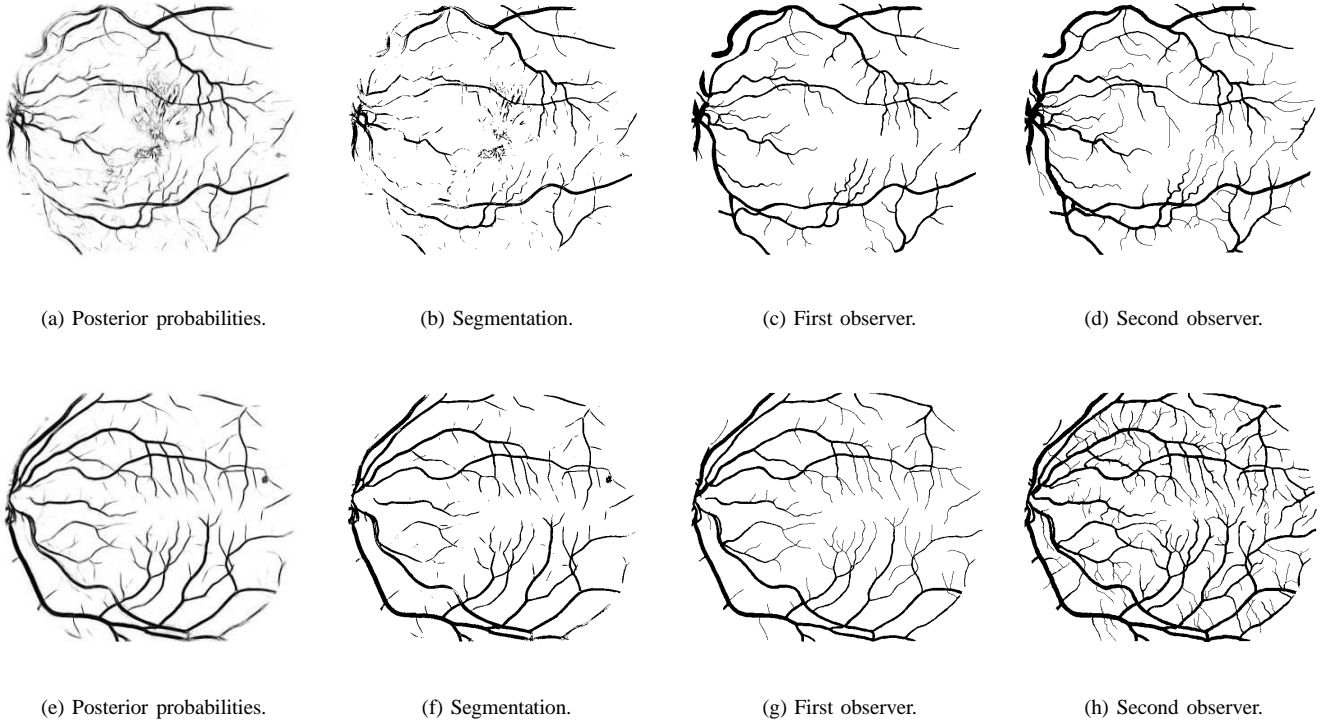


Fig. 5. Results produced by the GMM classifier with $k = 20$ and manual segmentations for two images from the STARE database. The top row images originate from a pathological case, while the bottom ones originate from a normal case.

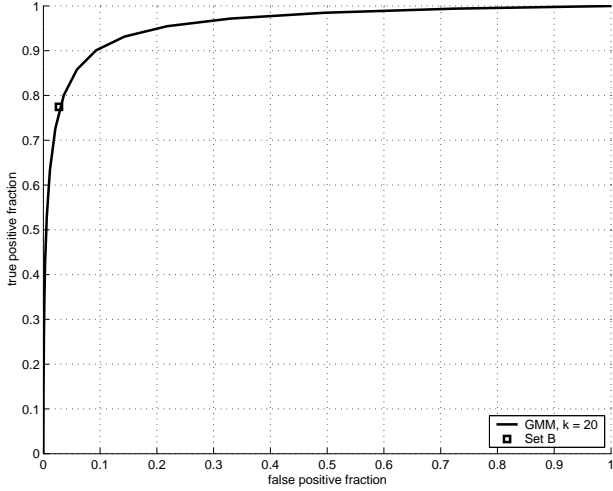


Fig. 6. ROC curve for classification on the DRIVE database using the GMM classifier with $k = 20$. The point marked as \blacksquare corresponds to set B, the second set of manual segmentations. The method has $A_z = 0.9598$.

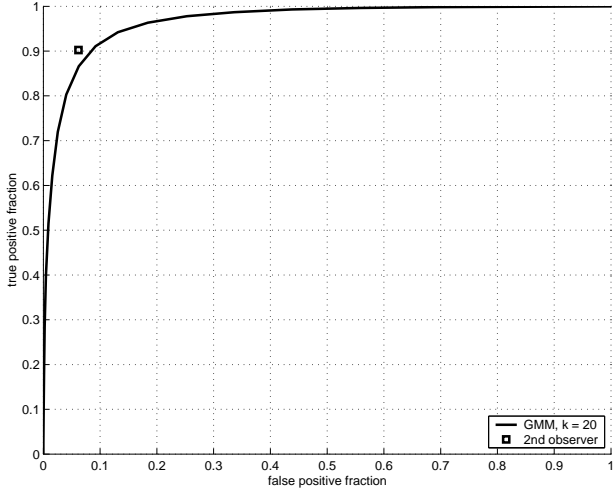


Fig. 7. ROC curve for classification on the STARE database using the GMM classifier with $k = 20$. The point marked as \blacksquare corresponds to the second observer's manual segmentations. The method has $A_z = 0.9651$.

TABLE I

RESULTS FOR DIFFERENT CLASSIFICATION METHODS AND HUMAN OBSERVER. A_z INDICATES THE AREA UNDER THE ROC CURVE, WHILE THE ACCURACY IS THE FRACTION OF PIXELS CORRECTLY CLASSIFIED.

Classification Method	Database			
	DRIVE		STARE	
	A_z	Accuracy	A_z	Accuracy
LMSE	0.9520	0.9280	0.9584	0.9362
GMM, $k = 1$	0.9250	0.9217	0.9394	0.9239
GMM, $k = 5$	0.9537	0.9431	0.9609	0.9430
GMM, $k = 10$	0.9570	0.9454	0.9627	0.9450
GMM, $k = 15$	0.9588	0.9459	0.9648	0.9470
GMM, $k = 20$	0.9598	0.9467	0.9651	0.9474
2nd. observer		0.9473		0.9349

Morlet transforms at different scales, which allows the segmentation of vessels of different diameters, are integrated through the use of the statistical classifiers presented. The LMSE classifier shows a reasonable performance with a fast classification and training phase, while the GMM classifier has a computationally demanding training phase, but guarantees a fast classification phase and better performance.

The classification framework demands the use of manual labelings, but allows the methods to be trained for different types of images (provided the corresponding manual segmentations are available), possibly adjusted to specific camera or lighting conditions and are otherwise automatic, i.e., adjustment of parameters or user interaction is not necessary. We are studying the use of training sets composed of a small portion of the image to be segmented. Using this approach, a semi-automated fundus segmentation software may be developed, in which the operator only has to draw a small portion of the vessels over the input image or simply click on several pixels associated with the vessels. The remaining image would then be segmented based on the partial training set. This approach is interesting since it requires a small effort from the operator, which is compensated by the fact that image peculiarities are directly incorporated by the classifier.

It is curious to note that, on the STARE database, the accuracy of the method is higher than that of the second observer (Table I). The second observer's manual segmentations contain much more of the thinnest vessels than the first observer (lowering their accuracy), while the method, trained by the first observer, is able to segment the vessels at a similar rate. However, the ROC graph (Fig. 7) still reflects the higher precision of the second observer, due to some difficulties found by the method, as discussed below.

It is possible to use only the skeleton of the segmentations for the extraction of features from the vasculature. Depending on the application, different evaluation methods become more appropriate [43]. For example, the evaluation of the skeleton would not take into account the width of the vessels, but could measure other qualities such as the presence of gaps and detection of branching points. Another interesting form of evaluation would be directly through an application, such as in detection of neovascularization by means of analysis and classification of the vessel structure [33]. A major difficulty in evaluating the results is the establishment of a reliable ground truth [44]. Human observers are subjective and prone to errors, resulting in large variability between observations. Thus, it is desirable that multiple human-generated segmentations be combined to establish a ground truth, which was not the case in the analysis presented.

Though very good ROC results are presented, visual inspection shows some typical difficulties of the method that must be solved by future work. The major errors are in false detection of noise and other artifacts. False detection occurs in some images for the border of the optic disc, haemorrhages and other types of pathologies that present strong contrast. Also, the method did not perform well for very large variations in lighting throughout an image, but this occurred for only one image out of the 40 tested from both databases. This could possibly be solved by including intra-image normalization

in the pre-processing phase [45]. Another difficulty is the inability to capture some of the thinnest vessels that are barely perceived by the human observers.

Another drawback of our approach is that it only takes into account information local to each pixel through image filters, ignoring useful information from shapes and structures present in the image. We intend to work on methods addressing this drawback in the near future. The results can be slightly improved through a post-processing of the segmentations for removal of noise and inclusion of missing vessel pixels as in [34]. An intermediate result of our method is the intensity image of posterior probabilities, which could possibly benefit from a threshold probing as in [2] or region growing schemes.

Automated segmentation of non-mydratic images provides the basis for automated assessment by community health workers. Skeletonized images of the vessel pattern of the ocular fundus can be analyzed mathematically using nonlinear methods such as global fractal [33] and local fractal [7] analysis based on the wavelet transform thus providing a numeric indicator of the extent of neovascularization. Our ongoing work aims at applying the shape analysis and classification strategies described in [33] to the segmented vessels produced by method described in this work.

ACKNOWLEDGMENTS

The authors thank J. J. Staal *et al.* [1] and A. Hoover *et al.* [2] for making their databases publicly available and Dr. Alan Luckie and Chris McQuellin from the Albury Eye Clinic for providing fluorescein images used during our research.

REFERENCES

- [1] J. J. Staal, M. D. Abramoff, M. Niemeijer, M. A. Viergever, and B. van Ginneken, "Ridge based vessel segmentation in color images of the retina," *IEEE Transactions on Medical Imaging*, vol. 23, no. 4, pp. 501–509, 2004.
- [2] A. Hoover, V. Kouznetsova, and M. Goldbaum, "Locating blood vessels in retinal images by piece-wise threshold probing of a matched filter response," *IEEE Transactions on Medical Imaging*, vol. 19, pp. 203–210, March 2000.
- [3] J. J. Kanski, *Clinical Ophthalmology: A systematic approach*. London: Butterworth-Heinemann, 1989.
- [4] E. J. Sussman, W. G. Tsiraras, and K. A. Soper, "Diagnosis of diabetic eye disease," *Journal of the American Medical Association*, vol. 247, pp. 3231–3234, 1982.
- [5] S. J. Lee, C. A. McCarty, H. R. Taylor, and J. E. Keeffe, "Costs of mobile screening for diabetic retinopathy: A practical framework for rural populations," *Aust J Rural Health*, vol. 8, pp. 186–192, 2001.
- [6] H. R. Taylor and J. E. Keeffe, "World blindness: a 21st century perspective," *British Journal of Ophthalmology*, vol. 85, pp. 261–266, 2001.
- [7] C. P. McQuellin, H. F. Jelinek, and G. Joss, "Characterisation of fluorescein angiograms of retinal fundus using mathematical morphology: a pilot study," in *5th International Conference on Ophthalmic Photography*, Adelaide, 2002, p. 152.
- [8] L. Streeter and M. J. Cree, "Microaneurysm detection in colour fundus images," in *Image and Vision Computing New Zealand*, Palmerston North, New Zealand, November 2003, pp. 280–284.
- [9] T. Y. Wong, W. Rosamond, P. P. Chang, D. J. Couper, A. R. Sharrett, L. D. Hubbard, A. R. Folsom, and R. Klein, "Retinopathy and risk of congestive heart failure," *Journal of the American Medical Association*, vol. 293, no. 1, pp. 63–69, 2005.
- [10] M. Niemeijer, J. J. Staal, B. van Ginneken, M. Loog, and M. D. Abramoff, "Comparative study of retinal vessel segmentation methods on a new publicly available database," in *SPIE Medical Imaging*, J. M. Fitzpatrick and M. Sonka, Eds., vol. 5370, 2004, pp. 648–656.
- [11] M. J. Cree, J. J. G. Leandro, J. V. B. Soares, R. M. Cesar-Jr., G. Tang, H. F. Jelinek, and D. J. Cornforth, "Comparison of various methods to delineate blood vessels in retinal images," in *Proc. of the 16th National Congress of the Australian Institute of Physics*, Canberra, Australia, 2005.
- [12] I. Liu and Y. Sun, "Recursive tracking of vascular networks in angiograms based on the detection-deletion scheme," *IEEE Transactions on Medical Imaging*, vol. 12, no. 2, pp. 334–341, 1993.
- [13] L. Zhou, M. S. Rzeszutarski, L. J. Singerman, and J. M. Chokreff, "The detection and quantification of retinopathy using digital angiograms," *IEEE Transactions on Medical Imaging*, vol. 13, no. 4, pp. 619–626, 1994.
- [14] O. Chutatape, L. Zheng, and S. M. Krishnan, "Retinal blood vessel detection and tracking by matched gaussian and kalman filters," in *Proc. of the 20th Annual International Conference of the IEEE Engineering in Medicine and Biology Society (EMBS'98)*, vol. 20, 1998, pp. 3144–3149.
- [15] Y. A. Tolias and S. M. Panas, "A fuzzy vessel tracking algorithm for retinal images based on fuzzy clustering," *IEEE Transactions on Medical Imaging*, vol. 17, pp. 263–273, April 1998.
- [16] A. Can, H. Shen, J. N. Turner, H. L. Tanenbaum, and B. Roysam, "Rapid automated tracing and feature extraction from retinal fundus images using direct exploratory algorithms," *IEEE Transactions on Information Technology in Biomedicine*, vol. 3, no. 2, pp. 125–138, 1999.
- [17] M. Lalonde, L. Gagnon, and M.-C. Boucher, "Non-recursive paired tracking for vessel extraction from retinal images," in *Proc. of the Conference Vision Interface 2000*, 2000, pp. 61–68.
- [18] X. Gao, A. Bharath, A. Stanton, A. Hughes, N. Chapman, and S. Thom, "A method of vessel tracking for vessel diameter measurement on retinal images," in *ICIP01*, 2001, pp. II: 881–884.
- [19] T. McInerney and D. Terzopoulos, "T-snakes: Topology adaptive snakes," *Medical Image Analysis*, vol. 4, pp. 73–91, 2000.
- [20] R. Toledo, X. Orriols, X. Binefa, P. Radeva, J. Vitria, and J. Villanueva, "Tracking of elongated structures using statistical snakes," in *IEEE Computer Society Conference on Computer Vision and Pattern Recognition (CVPR)*, vol. 1, 2000, p. 1157.
- [21] A. Vasilevskiy and K. Siddiqi, "Flux maximizing geometric flows," *IEEE Transactions on Pattern Analysis and Machine Intelligence*, pp. 1565–1578, 2002.
- [22] D. Nain, A. Yezzi, and G. Turk, "Vessel segmentation using a shape driven flow," in *Medical Image Computing and Computer-assisted Intervention - MICCAI*, 2004, pp. 51–59.
- [23] S. Chaudhuri, S. Chatterjee, N. Katz, M. Nelson, and M. Goldbaum, "Detection of blood vessels in retinal images using two-dimensional matched filters," *IEEE Transactions on Medical Imaging*, pp. 263–269, 1989.
- [24] L. Gang, O. Chutatape, and S. M. Krishnan, "Detection and measurement of retinal vessels in fundus images using amplitude modified second-order gaussian filter," *IEEE Transactions on Biomedical Engineering*, vol. 49, no. 2, pp. 168–172, 2002.
- [25] X. Jiang and D. Mojon, "Adaptive local thresholding by verification-based multithreshold probing with application to vessel detection in retinal images," *IEEE Transactions on Pattern Analysis and Machine Intelligence*, vol. 25, no. 1, pp. 131–137, 2003.
- [26] J. Lowell, A. Hunter, D. Steel, A. Basu, R. Ryder, and R. Kennedy, "Measurement of retinal vessel widths from fundus images based on 2-D modeling," *IEEE Transactions on Medical Imaging*, vol. 23, no. 10, pp. 1196–1204, October 2004.
- [27] F. Zana and J.-C. Klein, "Segmentation of vessel-like patterns using mathematical morphology and curvature evaluation," *IEEE Transactions on Image Processing*, vol. 10, pp. 1010–1019, 2001.
- [28] B. Fang, W. Hsu, and M. Lee, "Reconstruction of vascular structures in retinal images," in *ICIP03*, 2003, pp. II: 157–160.
- [29] M. E. Martínez-Pérez, A. D. Hughes, A. V. Stanton, S. A. Thom, A. A. Bharath, and K. H. Parker, "Retinal blood vessel segmentation by means of scale-space analysis and region growing," in *Medical Image Computing and Computer-assisted Intervention - MICCAI*, 1999, pp. 90–97.
- [30] R. Nekovei and Y. Sun, "Back-propagation network and its configuration for blood vessel detection in angiograms," *IEEE Transactions on Neural Networks*, vol. 6, no. 1, pp. 64–72, 1995.
- [31] C. Sinthanayothin, J. Boyce, and C. T. Williamson, "Automated localisation of the optic disc, fovea, and retinal blood vessels from digital colour fundus images," *British Journal of Ophthalmology*, vol. 83, pp. 902–910, 1999.
- [32] J. J. G. Leandro, R. M. Cesar-Jr., and H. Jelinek, "Blood vessels segmentation in retina: Preliminary assessment of the mathematical morphology

- and of the wavelet transform techniques,” in *Proc. of the 14th Brazilian Symposium on Computer Graphics and Image Processing*. IEEE Computer Society, 2001, pp. 84–90.
- [33] H. F. Jelinek and R. M. Cesar-Jr., “Segmentation of retinal fundus vasculature in non-mydratic camera images using wavelets,” in *Angiography and Plaque Imaging: Advanced Segmentation Techniques*, J. Suri and T. Laxminarayan, Eds. CRC Press, 2003, pp. 193–224.
 - [34] J. J. G. Leandro, J. V. B. Soares, R. M. Cesar-Jr., and H. F. Jelinek, “Blood vessels segmentation in non-mydratic images using wavelets and statistical classifiers,” in *Proc. of the 16th Brazilian Symposium on Computer Graphics and Image Processing*. IEEE Computer Society Press, 2003, pp. 262–269.
 - [35] O. Rioul and M. Vetterli, “Wavelets and signal processing,” *IEEE Signal Processing Magazine*, pp. 14–38, Oct. 1991.
 - [36] L. da F. Costa and R. M. Cesar-Jr., *Shape analysis and classification: theory and practice*. CRC Press, 2001.
 - [37] A. Grossmann, “Wavelet transforms and edge detection,” in *Stochastic Processes in Physics and Engineering*, S. A. et al., Ed. D. Reidel Publishing Company, 1988, pp. 149–157.
 - [38] J.-P. Antoine, P. Carette, R. Murenzi, and B. Piette, “Image analysis with two-dimensional continuous wavelet transform,” *Signal Processing*, vol. 31, pp. 241–272, 1993.
 - [39] R. S. Feris, V. Krueger, and R. M. Cesar-Jr., “A wavelet subspace method for real-time face tracking,” *Real-Time Imaging*, vol. 10, pp. 339–350, 2004.
 - [40] A. Arnéodo, N. Decoster, and S. G. Roux, “A wavelet-based method for multifractal image analysis. i. methodology and test applications on isotropic and anisotropic random rough surfaces,” *The European Physical Journal B*, vol. 15, pp. 567–600, 2000.
 - [41] S. Theodoridis and K. Koutroumbas, *Pattern Recognition*, 1st ed. USA: Academic Press, 1999.
 - [42] R. O. Duda, P. E. Hart, and D. G. Stork, *Pattern Classification*. John Wiley and Sons, 2001.
 - [43] K. W. Bowyer and P. J. Phillips, Eds., *Empirical Evaluation Techniques in Computer Vision*. IEEE Computer Society, 1998.
 - [44] K. H. Fritzsche, A. Can, H. Shen, C.-L. Tsai, J. N. Turner, H. L. Tanenbaum, C. V. Stewart, and B. Roysam, “Automated model-based segmentation, tracing, and analysis of retinal vasculature fom digital fundus images,” in *Angiography and Plaque Imaging: Advanced Segmentation Techniques*, J. Suri and S. Laxminarayan, Eds. CRC Press, 2003, pp. 225–297.
 - [45] M. J. Cree, E. Gamble, and D. Cornforth, “Colour normalisation to reduce interpatient and intra-patient variability in microaneurysm detection in colour retinal images,” in *WDIC2005 ARPS Workshop on Digital Image Computing*, Brisbane, Australia, February 2005, pp. 163–168.